

# Satellite tidal magnetic signals constrain oceanic lithosphere-asthenosphere boundary

**Grayver, Alexander V.; Schnepf, Neesha R.; Kuvshinov, Alexey V.; Sabaka, Terence J.; Manoj, Chandrasekharan; Olsen, Nils**

*Published in:*
Science Advances

*Link to article, DOI:*
10.1126/sciadv.1600798

*Publication date:*
2016

*Document Version*
Publisher's PDF, also known as Version of record

GEOPHYSICS


10.1126/sciadv.1600798

# Satellite tidal magnetic signals constrain oceanic lithosphere-asthenosphere boundary

**Alexander V. Grayver,[1]* Neesha R. Schnepf,[2] Alexey V. Kuvshinov,[1] Terence J. Sabaka,[3] Chandrasekharan Manoj,[4] Nils Olsen[5]**

**The tidal flow of electrically conductive oceans through the geomagnetic field results in the generation of secondary magnetic signals, which provide information on the subsurface structure. Data from the new generation of satellites were shown to contain magnetic signals due to tidal flow; however, there are no reports that these signals have been used to infer subsurface structure. We use satellite-detected tidal magnetic fields to image the global electrical structure of the oceanic lithosphere and upper mantle down to a depth of about 250 km. The model derived from more than 12 years of satellite data reveals a ≈72-km-thick upper resistive layer followed by a sharp increase in electrical conductivity likely associated with the lithosphere-asthenosphere boundary, which separates colder rigid oceanic plates from the ductile and hotter asthenosphere.**

## INTRODUCTION

Electrical conductivity (the reciprocal of resistivity) provides a wealth of information on the thermal and compositional state of Earth's mantle (*1*, *2*), with high sensitivity to small fractions of conductive phases, such as fluids and partial melts. Conventionally, the electrical structure of the oceanic lithosphere and upper mantle has been studied with seafloor magnetotelluric (MT) sounding using natural ionospheric excitation sources (*3*–*5*). Recent progress in the quality of satellite data, as well as processing and modeling techniques, now allows us to use another natural source: ocean tidal flow. Secondary electromagnetic (EM) fields produced by the electrically conductive seawater flowing through the ambient geomagnetic field obey Maxwell's equations

$$\begin{aligned} \mu^{-1}\nabla\times\vec{B} &= \sigma\vec{E}+\vec{j}^{\,\mathrm{ext}} \\ \nabla\times\vec{E} &= i\omega\vec{B} \end{aligned} \quad (1)$$

where $\vec{E}$ and $\vec{B}$ are electric and magnetic fields, respectively; μ and σ are magnetic permeability and electrical conductivity of the medium, respectively; ω is the angular frequency; and $\vec{j}^{\,\mathrm{ext}}$ is the extraneous current due to tidal flow given by

$$\vec{j}^{\,\mathrm{ext}} = \sigma_s(\vec{v}\times\vec{B}^{\,\mathrm{main}}) \quad (2)$$

Here, $\sigma_s$ is the conductivity of seawater (Fig. 1D), $\vec{B}^{\,\mathrm{main}}$ is Earth's main (core) magnetic field (Fig. 1, A to C), and $\vec{v}=\vec{u}/h$, where $h$ is the height of the water column and $\vec{u}$ is the depth-integrated seawater velocity due to tidal forces (Fig. 1, E and F)—a parameter that is well constrained by modern high-resolution assimilated global models of deep ocean tides (*6*, *7*). In contrast to previous synthetic studies (*8*–*10*), all quantities—including $\sigma_s$—in Eq. 2 vary laterally. The phenomenon described by Eqs. 1 and 2 is known as "motional induction" (*11*, *12*).

It was shown that satellite data contain measurable magnetic signals due to tidal flow (*8*, *9*), and these signals have sensitivity to subsurface structures (*13*). Attempts have been made to estimate bulk electrical properties of the subsurface using motionally induced EM signals recorded at isolated locations on land and on the seafloor (*14*, *15*). These signals have also been used in ocean circulation studies (*16*), but their use for sounding Earth's conductivity was not reported to date.

Earth sounding with satellite-detected tidal magnetic signals differs from conventional EM sounding in several ways. Conventional methods, such as MT, rely on a broad frequency content of the detected natural EM variations, whereas the tidal signal is limited to the frequency of the corresponding tide. By analogy with techniques, such as electrical impedance tomography (*17*), the sounding is still possible because of the spatially heterogeneous nature of the extraneous currents generated in the oceans and because induced secondary magnetic fields can be detected at multiple locations (for instance, at satellites). Another distinguishing feature is the galvanic coupling of the oceans with the seafloor. Methods with a purely inductive excitation mechanism (based on EM variations in the ionosphere or magnetosphere) are generally weakly influenced by the toroidal part of the exciting field. This leads to reduced sensitivity for resistive structures in the subsurface (*18*). In contrast, detected tidal magnetic signals (*14*) include this component through galvanic coupling and interaction of the induced fields with lateral inhomogeneities.

## RESULTS

The availability of more than 12 years of satellite and magnetic observatory data (*19*) enabled us to reliably extract the magnetic field due to the principal lunar semidiurnal ($M_2$) tidal constituent (Fig. 2A) as a data set with unprecedented globally uniform spatial coverage. At a satellite altitude of 430 km, the tidal field has a maximum amplitude of 2.1 nT, which is a relatively weak signal compared to the maximum total magnetic field intensity at that height (up to 54,000 nT). Nevertheless, observed tidal magnetic signals cannot be explained with

[1]Institute of Geophysics, ETH Zürich, Sonneggstrasse 5, Zürich, Switzerland. [2]Department of Geological Sciences/Cooperative Institute for Research In Environmental Sciences (CIRES), University of Colorado, Boulder, CO 80305–3337, USA. [3]Planetary Geodynamics Laboratory, NASA/Goddard Space Flight Center, Greenbelt, MD, USA. [4]National Oceanic and Atmospheric Administration's National Centers for Environmental Information/CIRES, University of Colorado, Boulder, CO 80305–3328, USA. [5]DTU Space, Lyngby, Denmark.
*Corresponding author. Email: agrayver@erdw.ethz.ch

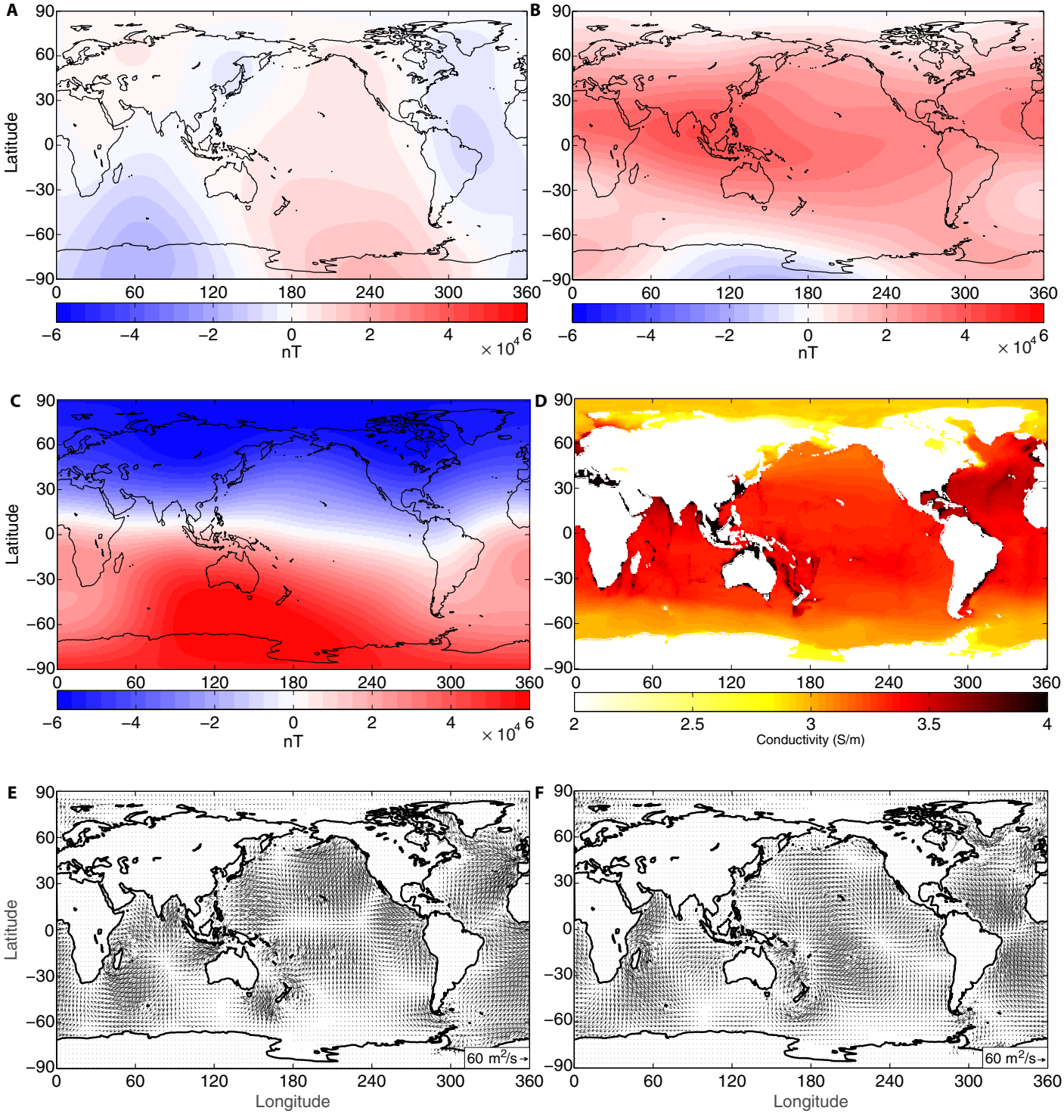


**Fig. 1. Input used to derive the extraneous electric current due to tidal flow (compare Eq. 2).** (**A** to **C**) Eastward, southward, and upward (radial) components of Earth's main (core) magnetic field for epoch 2010 (*23*). (**D**) Depth-averaged ocean water conductivity calculated for the year 2009 using global data of ocean salinity, temperature, and pressure. (**E** and **F**) In-phase and quadrature parts of the depth-integrated horizontal water velocity of $M_2$ tide (*7*). Note the scale in the right bottom corner.

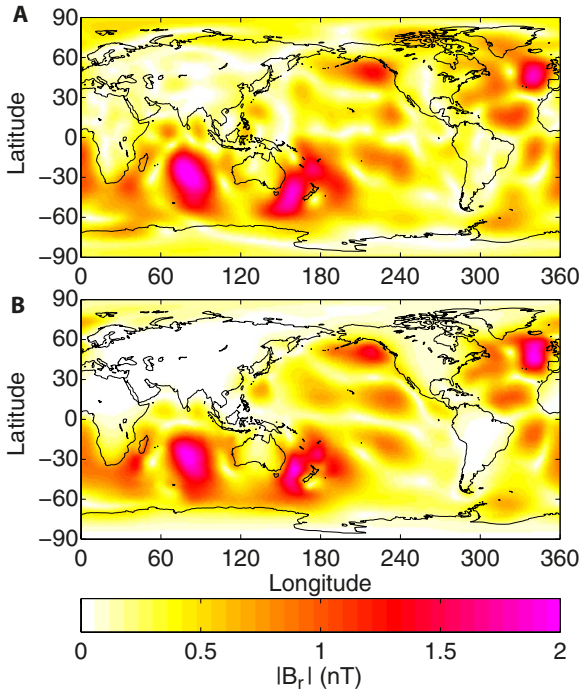


**Fig. 2. Amplitudes of the radial magnetic field components due to the $M_2$ tide at an altitude of 430 km.** (**A**) Extracted from satellite data. (**B**) Calculated on the basis of the recovered conductivity model (see structurally sparse model in Fig. 4).

an insulating or uniform lithosphere and mantle (Fig. 3, A and B), suggesting that more information about Earth's interior structure is contained in these signals. We inverted the observed magnetic field due to tidal flow to obtain a global radially variable conductivity model. The estimated model explains the observations remarkably well (Fig. 2B; see also movie S1). Because motional induction occurs in the oceans, we observe weaker signals over continents. However, the field above the continents is not strictly zero because the observations occur at satellite altitude, causing a portion of the signal to spread laterally.

Figure 4A illustrates the two best-fit radially varying conductivity models, as well as the conductivity of dry and water-saturated olivine (*1*) between depths of 80 and 400 km. We obtained the two models using different model constraints in the inversion algorithm. In the first case, smooth models were derived by minimizing differences between conductivities of the subsequent layers, whereas the second case results in structurally sparse models, by permitting sharp jumps in conductivity, but allowing as few features as possible. Both models explain the satellite observations almost equally well with the structurally sparse model-fitting data slightly better, although at this stage the difference is likely insignificant. The gray lines denote models whose misfit differs from the best-fit models by ≤10%. Considering the model uncertainty, the dry and water-saturated olivine curves bracket the structurally sparse model within the entire depth range. However, the smooth model has lower conductivity in the range of 100 to 150 km. Another prominent difference between the models is the conductivity jump observed at a depth of 72 km in the structurally sparse model. Low-misfit models indicate that the data fit varies insignificantly if the depth of this jump changes within 10 to 15 km. This jump can be associated with the lithosphere-asthenosphere boundary (LAB). Multiple seismic studies concluded that the average oceanic LAB depth occurs in a depth range of 70 to 80 km (*20*, *21*). Above the LAB, the colder rigid lithosphere is more resistive, whereas the asthenosphere is significantly more conductive because of its higher temperatures, as well as enhancements due to other mechanisms, such as partial melt and water (*3*, *5*). Because the smooth model must respect the imposed smoothing constraints, it does not exhibit any jump at these depths. Assuming that the structurally sparse model represents a plausible scenario, the enhanced conductivity of the asthenosphere suggests abundance of partial melts and water in the upper mantle.

Figure 4B compares our resulting models with a range of local models obtained via seafloor MT sounding for different geological settings (*4*, *22*), relying on natural EM variations that originate in the ionosphere. This is a completely different and independent type of excitation than the motional induction due to tides used in this study. All MT models show conductive material concentrated immediately below the seafloor, corresponding to the water-saturated floor sediments, which affect obtained models at greater depths because of smoothing regularization used. Our models do not have this feature because we incorporated sediments a priori (see Materials and Methods). Depending on the age of the underlying plate, the MT models show variable lithosphere thickness and increased conductivity below the LAB. At a depth of 250 km, all models are practically the same, given model uncertainty at these depths (*4*). Note that the rather homogeneous character of our models below the 250-km depth is likely associated with the low sensitivity of the tidal data to regions beyond these depths and should be interpreted with caution.

Several factors contribute to the uncertainty of the obtained models. Among them is the noise in the observed signal and error in the extraneous current defined by Eq. 2. The latter is calculated using the World Magnetic Model (WMM) (*23*), the HAMTIDE ocean tidal model (*7*), and laterally variable ocean electrical conductivity derived from ocean salinity and temperature data given by the World Ocean Atlas 2009. Uncertainty in these models will propagate to the modeled magnetic fields and can affect upper mantle conductivity models. To ensure reliability of the electrical conductivity models, variance in the modeled magnetic field signals due to uncertainty in the source needs to be below data's noise level. Unfortunately, little quantitative information is available about uncertainty of the aforementioned models, making a rigorous error propagation analysis difficult to implement. Instead, we performed a series of sensitivity tests, considering key factors for each of the quantities in Eq. 2. We compared tidal magnetic signals modeled using HAMTIDE and TPXO8-atlas—two independent and widely used data-assimilated tidal models. Although these models are independent, they use many similar data to estimate tidal flow; thus, the possibility of some peculiar systematic shift cannot be fully ruled out. On the other hand, because data-assimilated tidal models lack uncertainty information on the estimated tidal flow (*24*), this seems to be a reasonable way to obtain a proxy for their error. Figure 5A shows the absolute difference between radial magnetic field components calculated using both tidal models. The differences are below the current noise level in the observed data.

The effect of laterally variable ocean conductivity (LVOC) is more significant, as can be seen in Fig. 5B, showing absolute difference between radial magnetic field components calculated using a constant ocean conductivity of 3.2 S/m and LVOC derived in this study (Fig. 1D), justifying the usage of LVOC for inversion. LVOC is based on World Ocean Atlas data and equation of state (*25*), both leading to uncertainty

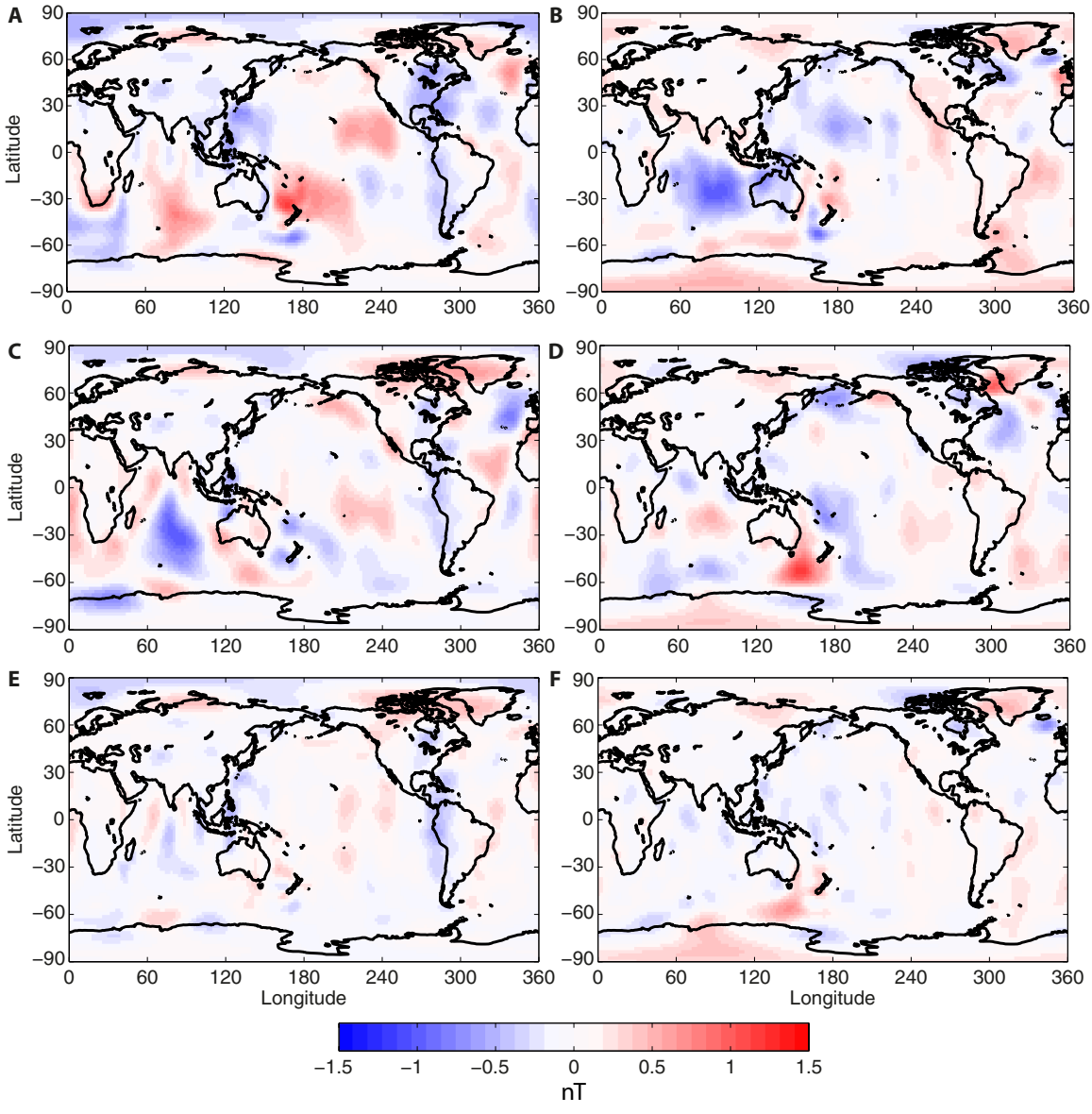


**Fig. 3. Difference between observed and predicted in-phase (left) and quadrature (right) radial magnetic field components due to the tidal flow at the satellite altitude (430 km).** (**A** and **B**) For an insulating mantle. (**C** and **D**) For a homogeneous mantle of 0.2 S/m conductivity (used as an initial guess for the inversion). (**E** and **F**) For the structurally sparse model shown in Fig. 4.

in the LVOC. World Ocean Atlas does not provide uncertainty on its data, making it hard to estimate errors in the LVOC. To overcome this, we assume that LVOC uncertainty is on the order of seasonal variations in LVOC, which can reach 0.2 S/m. Figure 5C shows the absolute difference in responses calculated for the annual average LVOC (Fig. 1D) and the Northern Hemisphere winter LVOC. The difference is below 0.02 nT, making this factor negligible. Finally, uncertainty in the main magnetic field $\vec{B}^{\text{main}}$ may also play a role. The global uncertainty for the WMM is estimated to be ≈150 nT, largely coming from omission of other field components, such as those due to lithosphere and ionosphere (*23*). Compared to the total field intensity, this error appears very small. Figure 5D shows the absolute difference between the modeled response and the extraneous current incorporating a lithosphere field that can reach few hundreds of nanotesla in the oceans. As anticipated, the difference is negligible, allowing us to model tidal magnetic signals with sufficiently high accuracy.

## DISCUSSION AND CONCLUSIONS

We demonstrated that tidal magnetic signals detected by satellites can be used to retrieve information on the electrical structure of the upper mantle. Initial residual fields were substantially reduced, and the derived model explains the data well (Fig. 3). With a data uncertainty of 0.15 nT,

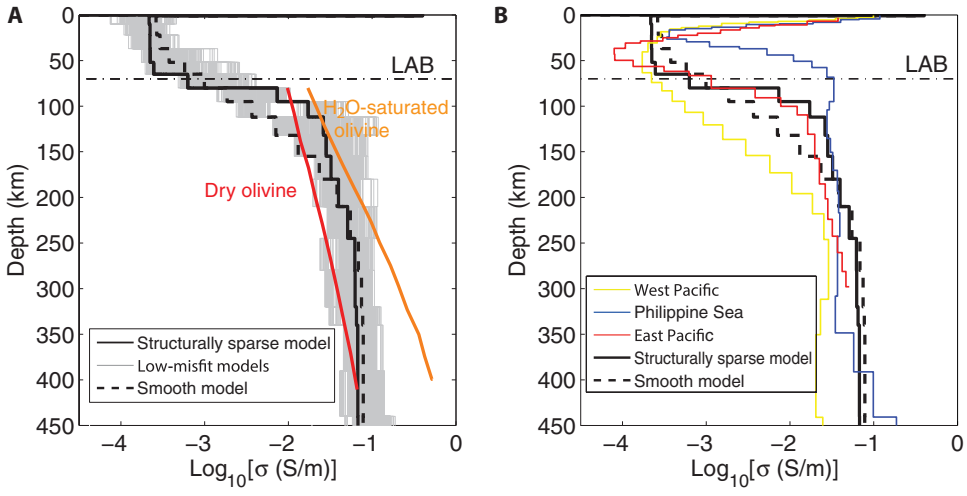


**Fig. 4. The recovered global radial electrical conductivity models compared with mineral physics constraints and local models derived from seafloor MT data.** (**A**) Black solid and dashed lines represent the most probable models obtained by using structurally sparse (that is, permit conductivity jumps but allow as few features as possible) and smooth constraints in the inversion algorithm, respectively (*35*). The gray lines denote the 1000 models for which misfit differs no more than 10% from the most probable solutions. Conductivities of the dry and water-saturated olivine (*1*) are shown with red and orange lines, respectively. (**B**) The blue line represents the conductivity model from the Philippine Sea plate [<60 million years old (Ma)] (*4*), whereas the red curve represents that from the East Pacific region (70 Ma) (*22*) and the yellow line shows that from the West Pacific region (125 to 150 Ma) (*4*). The horizontal dash-dotted line marks the average oceanic LAB depth estimated from seismic data (*21*).

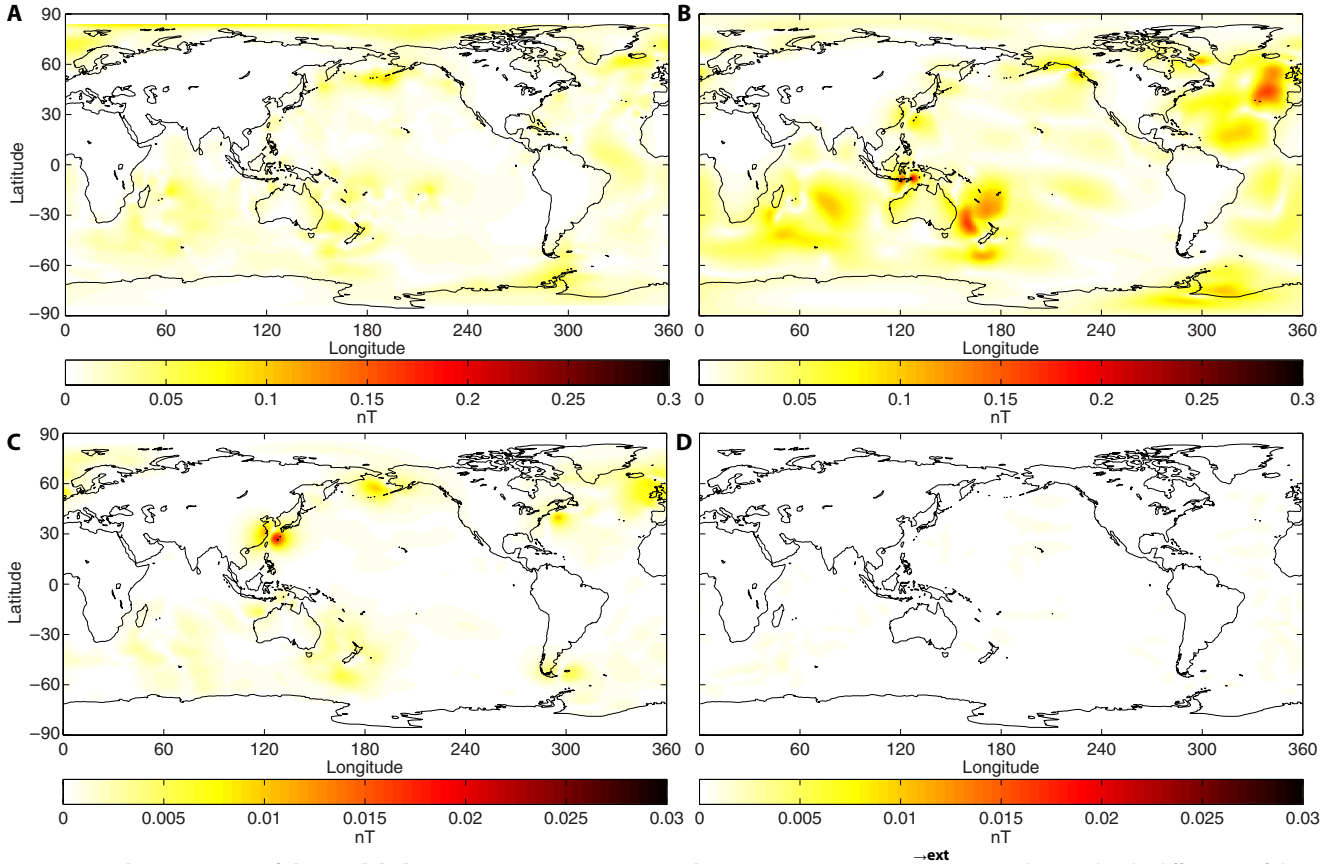


**Fig. 5. Testing the sensitivity of the modeled responses to uncertainty in the extraneous current $\vec{j}^{ext}$ term.** The amplitude difference of the radial magnetic field component between models using extraneous current constructed with (**A**) TPXO8-atlas and HAMTIDE tidal models, (**B**) a constant ocean electrical conductivity of 3.2 S/m and LVOC shown in Fig. 1D, (**C**) seasonally averaged conductivity (Fig. 1D) and Northern Hemisphere winter ocean conductivity, and (**D**) core field and core plus lithosphere fields. All fields are calculated at an altitude of 430 km. The recovered structurally sparse model (Fig. 4) was used as a mantle conductivity profile for these tests. Note the different scales.

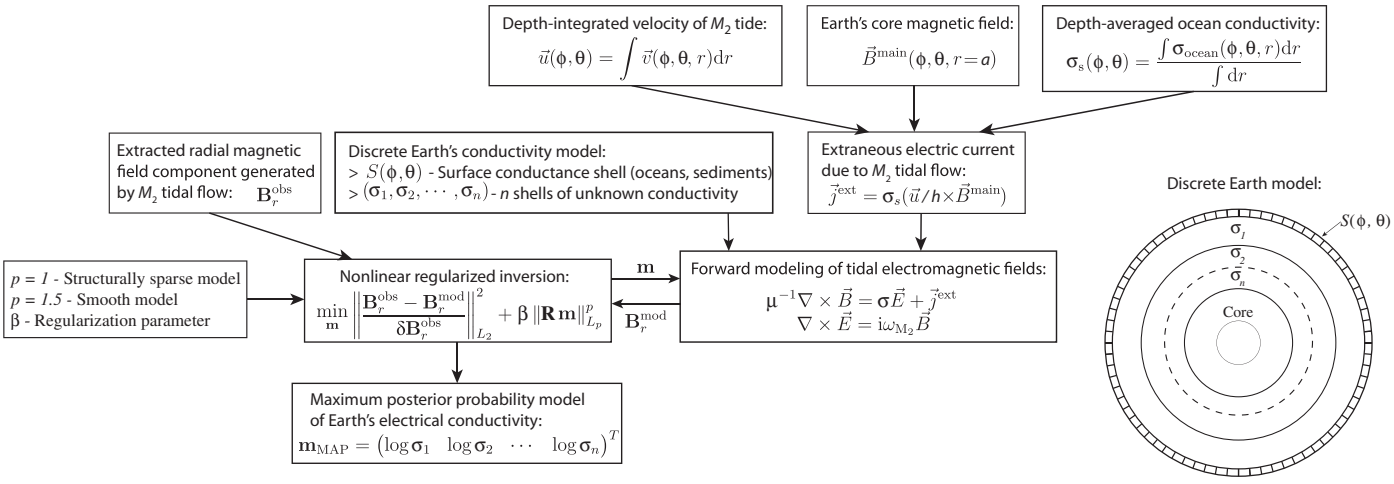


**Fig. 6. Workflow diagram showing principal steps and dependencies used to derive electrical conductivity models from satellite-detected tidal magnetic signals.** ϕ, θ, and *r* are spherical coordinates. All quantities, except scalars *p*, β, and $\sigma_{1\ldots n}$, are defined on a global grid and depend on ϕ and θ. Note that integrals $\int\ldots\mathrm{d}r$ imply integration along water column, which is $\int_a^{a-h(\phi,\theta)}\ldots\mathrm{d}r$.

the presented models have a normalized root mean square error of 1.05. The residuals between the extracted and modeled fields are zero-mean normally distributed, confirming that the derived model produces unbiased responses.

Our models provide the basis for a new constraint on upper mantle structure and can assist in mantle composition studies, which currently rely on seismic data and a limited number of regional electric models predominantly from the Pacific Ocean (*26*, *27*). One should consider, though, that the amplitude of the tidal magnetic signal and, hence, the amount of information about the subsurface that can be extracted from it vary laterally (Fig. 2). Therefore, derived models are more sensitive to the upper mantle structure in regions where signals are large. In addition, an average model tries to globally fit data, and the presented estimate of a LAB depth does not incorporate observed variations in the lithosphere thickness (*28*), be it due to cooling, the presence of partial melt, or other phenomena. Whether tidal magnetic signals can be used to map lateral variations in the upper mantle conductivity remains an open question and depends on the continued collection of high-quality satellite data (*29*).

The new approach presented here also offers a complement to the global deep sounding method, which lacks sensitivity to the upper mantle's resistive structures (*30*, *31*). The improved conductivity model can also be used for more accurate modeling of the ocean circulation magnetic signals (*16*). The strong tidal forces on moons with subsurface liquid oceans (such as Europa and Ganymede) (*32*), as well as the significant ambient magnetic fields around them (*33*), facilitate motional induction (*34*) and, provided that sufficiently long and accurate magnetic field measurements will be available, the detected tidal magnetic signals may become useful in constraining moons' inner structure.

## MATERIALS AND METHODS

### Data preparation

The extracted tidal magnetic signal was determined using a comprehensive inversion approach, where multiple components of the geomagnetic field (such as the core and crust) are coestimated (*19*). This obtained tidal field was compared with model values that depend on the extraneous current in the oceans, on ocean conductivity (provided as data file S1), and on the conductivity of the lithosphere and mantle.

The conductivity model was parameterized using a thin layer with a spatial resolution of 2° × 2° and 23 underlying homogeneous spherical layers of variable thickness (Fig. 6). A fixed surface conductance map that incorporates the conductivity of the continents, oceans, and seafloor sediments was used to account for the near-surface heterogeneous layer [as is shown by Kuvshinov (*10*)].

### Data inversion

A nonlinear regularized inversion method based on a global stochastic optimization algorithm was used (*35*) to convert the radial magnetic field component due to the $M_2$ tidal flow into a radial electrical conductivity model of the oceanic lithosphere and upper mantle. This was done by minimizing the misfit between the observed and modeled radial magnetic fields. Modeling of the EM fields was performed using the three-dimensional integral equation approach (*10*). Our detailed workflow is shown in Fig. 6.

To estimate the low-misfit models shown in Fig. 4A, we sampled 1000 models for which misfit does not differ by more than 10% from best-fit model misfit. This gave us a proxy for the uncertainty of the model. To perform this sampling, a two-step procedure was adopted. First, we found the most probable model and identified low-misfit regions of the model space. This was done by using the stochastic optimization algorithm called the covariance matrix adaptation evolution strategy (*36*). Second, using information obtained from the previous step, we drew samples from the equivalence domain by means of random sampling. In this case, equivalence domain is defined as a set of models in which the misfit is not significantly different from the best model misfit and still follows constraints imposed by the regularization (*35*).

## SUPPLEMENTARY MATERIALS

Supplementary material for this article is available at http://advances.sciencemag.org/cgi/content/full/2/9/e1600798/DC1

movie S1. Animation of the observed and predicted satellite magnetic tidal signals for Earth's principal lunar semidiurnal tide.

data file S1. A 1° × 1° map of depth-averaged ocean electric conductivity produced following the method of Fofonoff (*25*). The salinity and temperature data used are from National Oceanic and Atmospheric Administration's 2009 World Ocean Atlas annual climatology, whereas local pressure was estimated using the method of Saunders (*37*).

## REFERENCES AND NOTES


1. T. Katsura and T. Yoshino, Heterogeneity of electrical conductivity in the oceanic upper mantle, in *The Earth's Heterogeneous Mantle* (Springer International Publishing, 2015), pp. 173–204.
2. A. Khan, On Earth's mantle constitution and structure from joint analysis of geophysical and laboratory-based data: An example. *Surv. Geophys.* **37**, 149–189 (2016).
3. R. L. Evans, G. Hirth, K. Baba, D. Forsyth, A. Chave, R. Mackie, Geophysical evidence from the MELT area for compositional controls on oceanic plates. *Nature* **437**, 249–252 (2005).
4. K. Baba, H. Utada, T.-n. Goto, T. Kasaya, H. Shimizu, N. Tada, Electrical conductivity imaging of the Philippine Sea upper mantle using seafloor magnetotelluric data. *Phys. Earth Planet. In.* **183**, 44–62 (2010
5. S. Naif, K. Key, S. Constable, R. L. Evans, Melt-rich channel observed at the lithosphere–asthenosphere boundary. *Nature* **495**, 356–359 (2013).
6. G. D. Egbert, S. Y. Erofeeva, Efficient inverse modeling of barotropic ocean tides. *J. Atmos. Oceanic Tech.* **19**, 183–204 (2002).
7. E. Taguchi, D. Stammer, W. Zahel, Inferring deep ocean tidal energy dissipation from the global high-resolution data-assimilative HAMTIDE model. *J. Geophys. Res.* **119**, 4573–4592 (2014).
8. R. H. Tyler, S. Maus, H. Lühr, Satellite observations of magnetic fields due to ocean tidal flow. *Science* **299**, 239–241 (2003).
9. S. Maus, A. Kuvshinov, Ocean tidal signals in observatory and satellite magnetic measurements. *Geophys. Res. Lett.* **31**, L15313 (2004).
10. A. V. Kuvshinov, 3-D global induction in the oceans and solid earth: Recent progress in modeling magnetic and electric fields from sources of magnetospheric, ionospheric and oceanic origin. *Surv. Geophys.* **29**, 139–186 (2008).
11. A. D. Chave, D. S. Luther, Low-frequency, motionally induced electromagnetic fields in the ocean: 1. Theory. *J. Geophys. Res.* **95**, 7185–7200 (1990).
12. R. H. Tyler, L. A. Mysak, J. M. Oberhuber, Electromagnetic fields generated by a three dimensional global ocean circulation. *J. Geophys. Res.* **102**, 5531–5551 (1997).
13. N. R. Schnepf, A. Kuvshinov, T. Sabaka, Can we probe the conductivity of the lithosphere and upper mantle using satellite tidal magnetic signals? *Geophys. Res. Lett.* **42**, 3233–3239 (2015).
14. A. D. Chave, On the theory of electromagnetic induction in the Earth by ocean currents. *J. Geophys. Res.* **88**, 3531–3542 (1983).
15. A. Kuvshinov, A. Junge, H. Utada, 3-D modelling the electric field due to ocean tidal flow and comparison with observations. *Geophys. Res. Lett.* **33**, L06314 (2006).
16. C. Manoj, A. Kuvshinov, S. Maus, H. Lühr, Ocean circulation generated magnetic signals. *Earth Planets Space* **58**, 429–437 (2006).
17. M. Cheney, D. Isaacson, J. C. Newell, Electrical impedance tomography. *SIAM Rev.* **41**, 85–101 (1999).
18. E. B. Fainberg, A. V. Kuvshinov, B. S. Singer, Electromagnetic induction in a spherical Earth with non-uniform oceans and continents in electric contact with the underlying medium–II. Bimodal global geomagnetic sounding of the lithosphere. *Geophys. J. Int.* **102**, 283–286 (1990).
19. T. J. Sabaka, N. Olsen, R. H. Tyler, A. Kuvshinov, CM5, a pre-*Swarm* comprehensive geomagnetic field model derived from over 12 yr of CHAMP, Ørsted, SAC-C and observatory data. *Geophys. J. Int.* **200**, 1596–1626 (2015).
20. H. Kawakatsu, P. Kumar, Y. Takei, M. Shinohara, T. Kanazawa, E. Araki, K. Suyehiro, Seismic evidence for sharp lithosphere-asthenosphere boundaries of oceanic plates. *Science* **324**, 499–502 (2009).
21. C. A. Rychert, P. M. Shearer, A global view of the lithosphere-asthenosphere boundary. *Science* **324**, 495–498 (2009).
22. E. Sarafian, R. L. Evans, J. A. Collins, J. Elsenbeck, G. A. Gaetani, J. B. Gaherty, G. Hirth, D. Lizarralde, The electrical structure of the central Pacific upper mantle constrained by the NoMelt experiment. *Geochem. Geophys. Geosyst.* **16**, 1115–1132 (2015).
23. A. Chulliat, S. Macmillan, P. Alken, C. Beggan, M. Nair, B. Hamilton, A. Woods, V. Ridley, S. Maus, A. Thomson, *The US/UK World Magnetic Model for 2015-2020: Technical Report* (National Geophysical Data Center, National Oceanic and Atmospheric Administration, 2015).
24. D. Stammer, R. D. Ray, O. B. Andersen, B. K. Arbic, W. Bosch, L. Carrère, Y. Cheng, D. S. Chinn, B. D. Dushaw, G. D. Egbert, S. Y. Erofeeva, H. S. Fok, J. A. M. Green, S. Griffiths, M. A. King, V. Lapin, F. G. Lemoine, S. B. Luthcke, F. Lyard, J. Morison, M. Müller, L. Padman, J. G. Richman, J. F. Shriver, C. K. Shum, E. Taguchi, Y. Yi, Accuracy assessment of global barotropic ocean tide models. *Rev. Geophys.* **52**, 243–282 (2014).
25. N. P. Fofonoff, Physical properties of seawater: A new salinity scale and equation of state for seawater. *J. Geophys. Res.* **90**, 3332–3342 (1985).
26. T. Yoshino, T. Matsuzaki, S. Yamashita, T. Katsura, Hydrous olivine unable to account for conductivity anomaly at the top of the asthenosphere. *Nature* **443**, 973–976 (2006).
27. D. Wang, M. Mookherjee, Y. Xu, S.-i. Karato, The effect of water on the electrical conductivity of olivine. *Nature* **443**, 977–980 (2006).
28. K. M. Fischer, H. A. Ford, D. L. Abt, C. A. Rychert, The lithosphere-asthenosphere boundary. *Annu. Rev. Earth Planet. Sci.* **38**, 551–575 (2010).
29. T. J. Sabaka, R. H. Tyler, N. Olsen, Extracting ocean-generated tidal magnetic signals from *Swarm* data through satellite gradiometry. *Geophys. Res. Lett.* **43**, 3237–3245 (2016).
30. A. Kelbert, A. Schultz, G. Egbert, Global electromagnetic induction constraints on transition-zone water content variations. *Nature* **460**, 1003–1006 (2009).
31. A. Semenov, A. Kuvshinov, Global 3-D imaging of mantle conductivity based on inversion of observatory *C*-responses—II. Data analysis and results. *Geophys. J. Int.* **191**, 965–992 (2012).
32. R. H. Tyler, Strong ocean tidal flow and heating on moons of the outer planets. *Nature* **456**, 770–772 (2008).
33. J. Saur, F. M. Neubauer, K.-H. Glassmeier, Induced magnetic fields in solar system bodies. *Space Sci. Rev.* **152**, 391–421 (2010).
34. K. K. Khurana, M. G. Kivelson, K. P. Hand, C. T. Russell, *Electromagnetic Induction from Europa's Ocean and the Deep Interior* (The University of Arizona Space Science Series, University of Arizona Press, 2009), p. 571.
35. A. V. Grayver, A. V. Kuvshinov, Exploring equivalence domain in nonlinear inverse problems using Covariance Matrix Adaption Evolution Strategy (CMAES) and random sampling. *Geophys. J. Int.* **205**, 971–987 (2016).
36. N. Hansen, A. Ostermeier, Completely derandomized self-adaptation in evolution strategies. *Evol. Comput.* **9**, 159–195 (2001).
37. P. M. Saunders, Practical conversion of pressure to depth. *J. Phys. Oceanogr.* **11**, 573–574 (1981).



**Acknowledgments**

**Funding:** This work is supported by the European Space Agency STSE (Support To Science Element) Swarm + Innovation Program (European Space Research and Technology Centre contract no. 4000113885/15/NL/MP). **Author contributions:** A.V.G. conducted the data inversion and analyzed the results; A.V.K. provided three-dimensional forward modeling code; T.J.S. and N.O. processed and prepared satellite data; N.R.S. prepared extraneous electric current maps; and N.R.S. and C.M. compiled depth-averaged seawater conductivity map. A.V.G., A.V.K., and N.R.S. designed the study, and A.V.G. drafted the manuscript. All authors discussed the results and commented on the manuscript. **Competing interests:** The authors declare that they have no competing interests. **Data and materials availability:** All data needed to evaluate the conclusions in the paper are present in the paper and/or the Supplementary Materials. Additional data related to this paper may be requested from the authors.

Submitted 14 April 2016
Accepted 24 August 2016
Published 30 September 2016
10.1126/sciadv.1600798

**Citation:** A. V. Grayver, N. R. Schnepf, A. V. Kuvshinov, T. J. Sabaka, C. Manoj, N. Olsen, Satellite tidal magnetic signals constrain oceanic lithosphere-asthenosphere boundary. *Sci. Adv.* **2**, e1600798 (2016).

ScienceAdvances
AAAS

# Satellite tidal magnetic signals constrain oceanic lithosphere-asthenosphere boundary

Alexander V. Grayver, Neesha R. Schnepf, Alexey V. Kuvshinov, Terence J. Sabaka, Chandrasekharan Manoj and Nils Olsen

(September 30, 2016)
*Sci Adv* 2016, 2:.
doi: 10.1126/sciadv.1600798